Evaluation of electromagnetic performance of emerging failures in electrical machines using computational simulation

Jose Rafael Guzman-Sepulveda & Rafael Guzman-Cabrera

Electrical Engineering
Archiv für Elektrotechnik

ISSN 0948-7921

Electr Eng
DOI 10.1007/s00202-017-0604-5

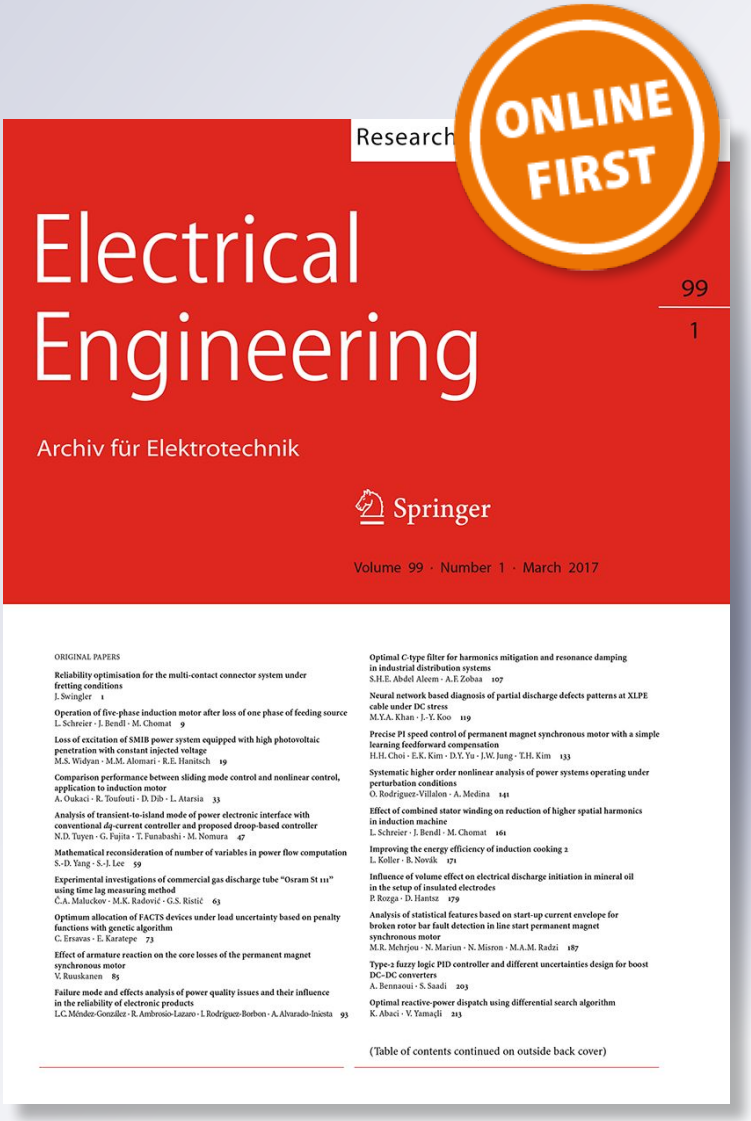

Springer

Electr Eng
DOI 10.1007/s00202-017-0604-5

ORIGINAL PAPER

Evaluation of electromagnetic performance of emerging failures in electrical machines using computational simulation

Jose Rafael Guzman-Sepulveda[1] · **Rafael Guzman-Cabrera**[2]

Received: 14 February 2015 / Accepted: 10 July 2017

Abstract Common failures in industrial induction motors equipped with squirrel cage rotor are examined in this paper. These failures are: broken rotor bars and short circuit in the inter-turn winding. The broken rotor bars failure was simulated with two consecutive broken bars in order to see how the magnetic flux density is affected. The inter-turn short circuit was simulated with 40% reduction of winding coil in an inter-turn short circuit, for one of the phases. The waveform of the flux density was plotted directly, while the analysis of the harmonic distribution and its relation to the electrical failures was performed in the Fourier domain. The proposed methodology allows to clearly identify the fault conditions analyzed. Comparative test of the real failure was performed in order to verify the results obtained from the simulation; good agreement between simulation and experimental measurements was obtained.

Keywords Electromagnetic performance · Magnetic field simulation · Failure detection

1 Introduction

Most of the breakdowns in industrial induction motors are caused by three main reasons. First, failures in the bearings (41% of occurrence). This failure is easily identifiable due to an unique fingerprint: the noise produced when this failure occurs. The second most frequent failure in motors occurs in the winding stator (37%), but, unlike the previous case, this failure is much more complicated to identify because it takes place inside the motor. Finally, the third most frequent failure in AC motors is the breakage of the rotor bars (10%) [1,2]. This kind of failure is even more problematic and less likely to be detected than the stator failure, not only because special detection equipment is required, but also because the motor has to be out of line for corresponding tests to be performed. The detection of these failures is a matter of great importance because they are extremely difficult to detect if the appropriate equipment is not available [3,4].

All these failures have been widely studied, and several methods have been adopted in order to improve the detection techniques [5–7]. In this work, we propose a computational technique to model, process, and analyze the electrical signals related to the failures of inter-turn short circuit in the winding and the rotor's broken bars. The results obtained are a set of characteristics that enhance the reliable detection, diagnosis, and discrimination between all these failures.

1.1 Rotor broken bars

Previous works have demonstrated that broken bars originated from arduous duty cycles and they can be a major problem in certain induction motors [8]. Although broken rotor bars do not initially cause a motor failure, they can induce serious secondary effects. This can cause serious mechanical damage to the wiring insulation and consequently winding failures may occur, resulting in costly repairs and production halts.

Many previous publications have analyzed the theoretical performance of three-phase induction motors with broken rotor bars basing their findings on the symmetric magnetic field supplied by the stator [8,9]. The rotor current in cage

✉ Rafael Guzman-Cabrera
guzmanc@ugto.mx

Jose Rafael Guzman-Sepulveda
r.guzman@knights.ucf.edu

[1] CREOL, The College of Optics and Photonics, University of Central Florida, Orlando, FL 32816, USA

[2] Universidad de Guanajuato, Guanajuato, Mexico

Published online: 19 July 2017

winding produces an effective three-phase magnetic field rotating at a slip frequency (f_2) with respect to the rotating rotor. When the cage winding is symmetric, there is only a forward rotating field at a given slip frequency with respect to the rotor. The occurrence of rotor asymmetry will result in a backward rotating field with a slip frequency with respect to the forward rotating rotor [10]. The overall resulting effect is the induction of an electromagnetic force (EMF) and a current in the stator winding at a frequency:

$$f_{sb} = f_1(1 - 2s) \quad \text{Hz} \tag{1}$$

where f_{sb} is the slip frequency sideband with respect to the rotor, f_1 is the supply frequency (Hz), and s is per unit slip. This is known to be a twice slip frequency sideband due to the broken rotor bars. Therefore, a cyclic variation of the current causes a torque pulsation at twice slip frequency ($2sf_1$) and a corresponding speed oscillation that is also a function of the drive inertia. This speed oscillation can reduce the magnitude of the $f_1(1 - 2s)$ sideband, but a current upper sideband component of $f_1(1+2s)$ is induced in the stator winding due to rotor oscillations [6]. This upper sideband is also enhanced by the third harmonic flux.

1.2 Stator winding failures

The analysis of the air gap and the axial flux signals has been typically used to detect shorted turns in the winding. The mathematical formulations can be found in Ref. [11]. The components of the flux waveforms in the air gap, as a function of shorted inter-turns, are given by the following equation:

$$f_{st} = f_1[n/p(1 - s) \pm k] \tag{2}$$

where f_{st} represents the components as a function of shorted turns; f_1 is the supply frequency; n and k are constants; p is the amount of pole pairs; and s is the slip. If a short circuit in the winding occurs, a new path for the current circulation is formed. This new path causes a decrease of the coil impedance of the winding due to the reduction of the coil turns (i.e., turns that were in the series now are connected in parallel) [12,13]. The main consequence of this kind of failure is an increment of the total current flow through the shorted circuit winding. This additional current causes a temperature increase and then progressive failure of the insulation.

2 Finite element analysis (FEA)

Numerical simulations of the induction motor were performed by means of finite element analysis (FEA) in order to obtain graphical representations of the magnetic and electric fields distributions [14,15]. Using this kind of simulations accurate values of electric and magnetic fields can be calculated at each section of the motor, in such a way that qualitative and quantitative comparisons between the failure and non-failure conditions can be performed.

Table 1 Induction motor characteristics

Motor characteristics	Data
Power	7.5 HP
Connection	220 V Double star
Slots/coil	1–7
Turns	59
Coils/group	2
Slots	24
Voltage	208–230/460
Amp	3.2–3/1.5
Magnetic core length	2″1/2
Magnetic core diameter	3″1/8
Magnetic core inner diameter	1″9/16
Magnetic core outer diameter	2″12/16

Table 2 Materials used in the simulation

Section of the motor	Material
Rotor	M15 steel
Rotor bars'	Aluminum 6061 T6
Stator	M15 steel
Winding wire	Cu 22 AWG

2.1 Motor specifications

The electrical machine analyzed is an induction motor with squirrel cage rotor whose characteristics are shown in Table 1.

The materials used for FEA simulations are: Rotor M15 Steel, Rotor bars Aluminum 6061 T6, Stator M15 Steel, and Winding wire Cu 22 AWG. The general characteristics and magnetic properties are included in the simulation and are identified for each part of the motor. In order to simulate the winding's section, three electric circuits were created; the motor winding was connected to a double star in order to obtain a connection to 220 V (Table 2).

In order to evaluate the motor's performance, finite element simulations were performed for three representative cases where typical failures are encountered. These conditions are schematically illustrated in Fig. 1. The first condition refers to a motor under normal operation without failure (Fig. 1a); the second one represents a motor with broken rotor bars (Fig. 1b); and the third simulation represents a motor with 40% short circuit inter-turn in one phase of the

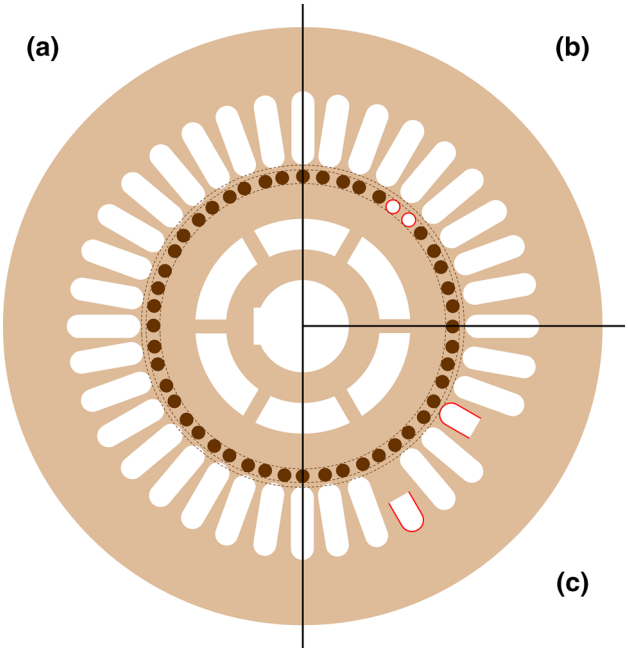

Fig. 1 Schematic of a single lamination of the rotor with squirrel cage where the three representative conditions related to failures commonly encountered are illustrated: **a** normal operation, **b** broken bars, and **c** 40% inter-turn short circuit

winding (Fig. 1c). In the simulations, the parameters for the motor were set according to the specifications and the materials mentioned above. The analysis of the magnetic flux in the air gap, between the rotor and the stator, can be done by considering the magnetic field performance in the middle of a single lamination. For the condition of operation without failure, the results for the flux density and the flux lines inside the stator core show no distortions neither in the air gap nor in the stator.

The "broken bar" condition was simulated by considering the absence of current in the bars of the motor. In this case, two consecutive bars were chosen for simulation purposes (see Fig. 1b). In this case, there is a clear distortion of the lines of the magnetic field distribution across the air gap, and this is caused by the broken bars, leading to a magnetic flux increase in the failure zone.

In order to simulate the failure in the inter-turn, one group of the winding was decreased by 40% for one phase. These failure zones for the phase A with a 40% turn reduction in the winding are indicated in Fig. 1c. In this case, the simulations show the same flux density distribution in the core as along the air gap in the failure zone. The magnetic flux distribution along the air gap is affected by the inter-turn reduction in the winding. The current density variation induced in the rotor causes a notorious imbalance due to the fault. As a consequence, a low magnetic flux density is generated and less amount of current is induced in the rotor failure zone.

Table 3 Confidence bounds results of different model evaluated

Model	R^2
Fourier 6 terms	0.8980
Fourier 7 terms	0.9093
Fourier 8 terms	0.9391
Sum sin functions	0.8995
Sum Gaussian functions	0.8820

Table 4 FFT coefficients for model of motor without failure (95% confidence bounds)

Term	Model of motor without failure	Model of motor with broken bars	Model of 40% inter-turn short circuit
$a0$	0.1301	0.1431	0.1265
$a1$	−0.0307	0.04608	−0.02887
$b1$	−0.06381	0.06659	−0.06495
$a2$	−0.04128	0.009971	−0.03986
$b2$	0.008838	0.04652	0.008351
$a3$	0.008351	−0.003122	0.008793
$b3$	0.02378	0.02502	0.02332
$a4$	0.022184	0.01316	0.02298
$b4$	0.02268	0.03765	0.02449
$a5$	0.007274	−0.02048	0.00725
$b5$	−0.02823	0.01978	−0.02782
$a6$	0.02236	0.02154	0.02198
$b6$	−0.00183	0.001227	0.002799
$a7$	−0.009127	0.01499	0.008328
$b7$	−0.007482	0.01105	0.007812
$a8$	0.0001895	0.01499	−0.0001516
$b8$	−0.01814	−0.008497	−0.0178
w	7.423	7.423	7.422

2.2 Data processing and analysis

Processing of the data obtained from the simulations was carried out by fitting to analytical expressions. One of the main goals, besides the qualitative comparison between the different conditions explored, based only on the identification of distorted flux lines, is to find analytical expressions that allow us to model the simulated results precisely and permit quantitative comparison by using specific parameters such as maximum, minimum, and fundamental frequencies, among others. In this particular case, the data obtained from the numerical simulations show characteristics strongly related to periodic features, which suggest that better performance will be obtained if the simulated data are modeled using periodic functions.

A wide variety of fitting models based on periodic functions can be found, the most common being those using

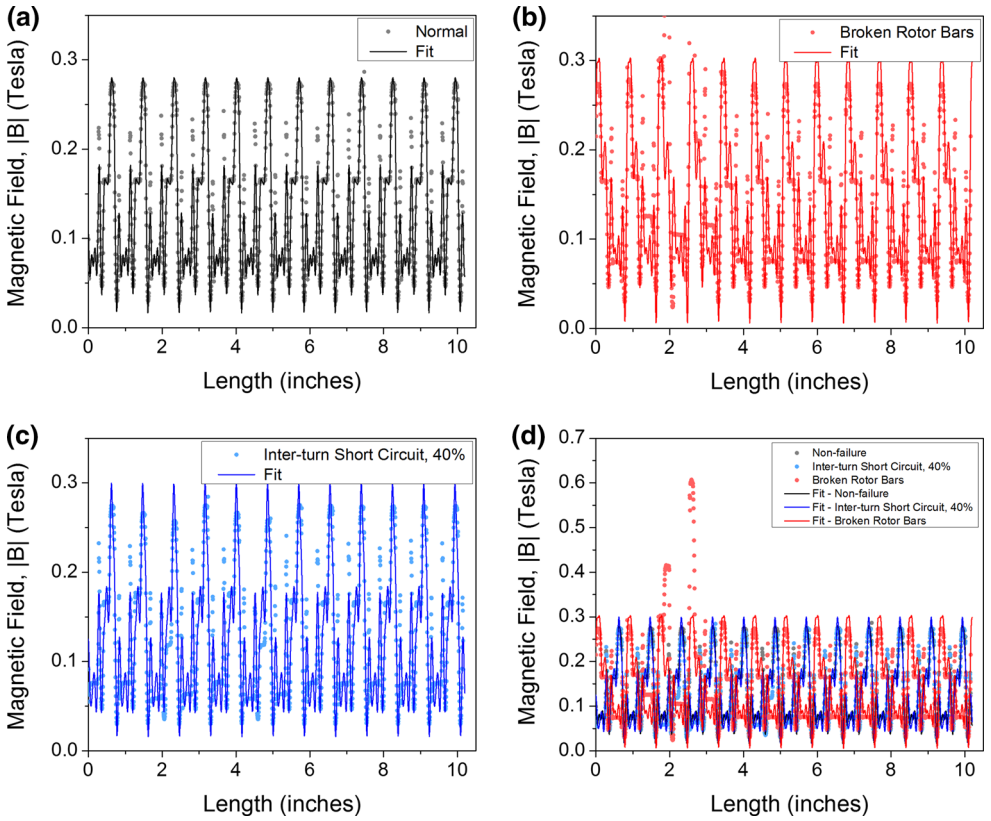

Fig. 2 Fit of the simulated data from **a** normal operation without failure, **b** broken bars, and **c** 40% inter-turn short circuit, to an 8-term Fourier series in all cases. **d** Overlap of all the simulated and fitted datasets, plot for comparison

Fourier like series. In this regard, Fourier series are not only the most common but also the ones that fit better the simulated results. Fourier series with different number of terms were explored for the data obtained from the numerical simulations and compared with other periodic functions like the Fourier sine series and the sum of Gaussian functions. It was found that an 8-terms Fourier series successfully models the simulated results with R^2 (R-square, coefficient of determination used to measure the accuracy of the model obtained) greater than 0.93. Table 3 shows the results obtained from the evaluation of different models considered, comparing R^2 data for all models evaluated.

The simulated data were fit to a general Fourier series with eight terms shown below in Eq. (3). This was the best model to fit the simulated data in all cases. The coefficients obtained from the fit, within 95% confidence bounds, are shown in Table 4 for all cases of study.

$$
\begin{aligned}
f(x) = {} & a0 + a1^* \cos(x^* w) + b1^* \sin(x^* w) \\
& + a2^* \cos(2^* x^* w) + b2^* \sin(2^* x^* w) \\
& + a3^* \cos(3^* x^* w) + b3^* \sin(3^* x^* w) \\
& + a4^* \cos(4^* x^* w) + b4^* \sin(4^* x^* w) \\
& + a5^* \cos(5^* x^* w) + b5^* \sin(5^* x^* w) \\
& + a6^* \cos(6^* x^* w) + b6^* \sin(6^* x^* w) \\
& + a7^* \cos(7^* x^* w) + b7^* \sin(7^* x^* w) \\
& + a8^* \cos(8^* x^* w) + b8^* \sin(8^* x^* w) \qquad (3)
\end{aligned}
$$

A summary of the fit is shown in Fig. 2. Clearly, the analytical model captures the relevant features of the different data sets and in all cases the model can be considered sufficient as it successfully describes the small peak components of the data. However, it is inaccurate for modeling the broken bars condition; specifically, there is a region where an outstanding peak appears.

In order to complement the fitting performed, the coefficients of the Fourier series are compared. The left and right figures below show the coefficients of the cosine and sine components, respectively. From Fig. 3, it can be clearly noticed that there is only a slight difference between the experiments labeled "Non-failure Condition" and "40% Inter-turn short circuit," while the experiment labeled "Broken Rotor Bars" is completely different to the other two. The coefficients of the cosine series present an oscillatory behavior in all the experiments, but the coefficients of "Broken Rotor Bars" seem to possess a larger damping factor when compared with the other two. This "damping factor" can be identified by the small delay between the experiments. On

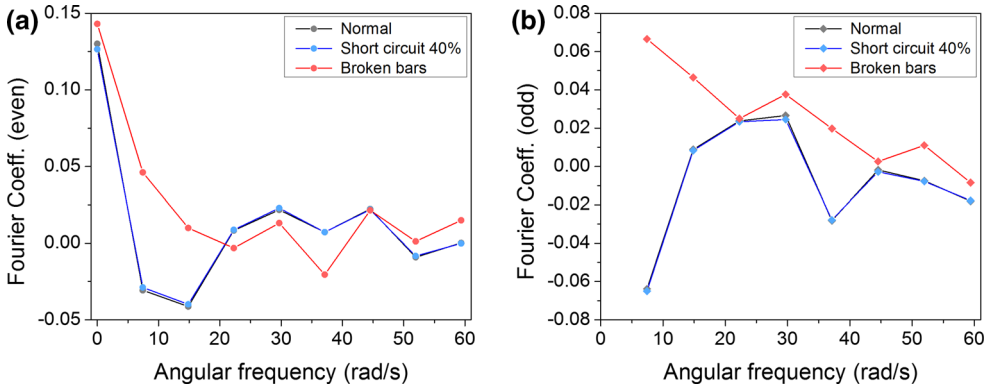

Fig. 3 Fourier series coefficients of the **a** cosine and **b** sine components for the three different conditions simulated

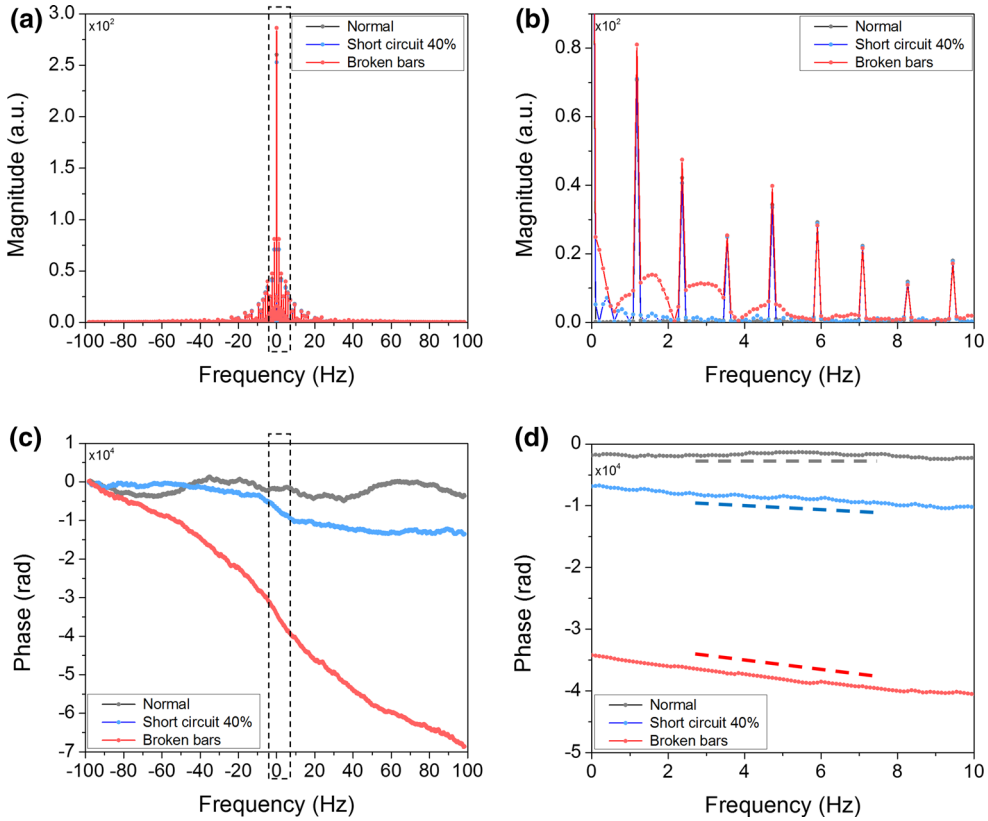

Fig. 4 **a**, **b** Magnitude and **c**, **d** phase of the direct Fourier transformation of the simulated datasets for the three different conditions. Panels (**a**) and (**c**), and (**b**) and (**d**) show the results for the full frequency range and for the low-frequency regime, respectively

the other hand, regarding the sine series, a difference in the sign of the coefficients appears for the first two components, which suggest a shift of the simulated data of "Broken Rotor Bars" with respect to the other two. This can be confirmed in Fig. 2, where it can be seen that the data from the "Broken Rotor Bars" are shifted from the other two experiments.

In order to provide better insight that allows discriminating between the different conditions, the simulated datasets were directly Fourier transformed. This is equivalent to decompose in a series like that in Eq. (3) with a much larger number of frequency components that include not only harmonics of a fundamental frequency but all frequencies within certain range. The magnitude and phase of the Fourier transformed data are shown in Fig. 4. Figure 4a, b shows the magnitude of the Fourier transform over the full frequency range taken and a zoomed-in region in the low-frequency region, respectively.

Similarly, Fig. 4c, d shows the same full-range and low-frequency plots, respectively, for the phase in the Fourier transform. This particular plots permit a clear discrimination between the different conditions simulated. The overall

magnitude of the phase is significantly different for the three conditions, but, more importantly, the plot reveals something else. It can be seen that for normal operation the phase across the spectrum is practically constant, while for the other two cases it is chirped. The amount of chirp is different for the two different failures, as indicated by the slope of the curves, and it can be seen that this chirp is more pronounced for the condition where the bars are broken.

3 Conclusions

In this work, we simulated, by means of a finite element approach, the performance of an electric motor with squirrel rotor cage for different operation conditions relating to failures commonly encountered. Three different conditions were chosen as representative: normal operation without failure, broken rotor bars, and 40% inter-turn short circuit.

In a first approach, the simulated datasets were described by using an 8-term Fourier series model. This was sufficient to capture the relevant features in the simulated datasets. Nevertheless, this analysis was not enough to clearly differentiate between all different conditions, specifically the "Non-failure Condition" and the "40% inter-turn short Circuit".

A better insight was obtained by directly Fourier-transforming the simulated datasets. In this case, it was shown that the phase of the Fourier transform allows a clear discrimination between the different conditions. This differentiation can be done based simply on the magnitude of the phase, but, more importantly, it was revealed that the spectral chirp (slope of the phase across the spectrum) is different for all three conditions. This feature can be used to extend a similar analysis to other types of failures for diagnosis purposes where specific failures can be identified by this phase signature.

References

1. Gandhi A, Corrigan T, Parsa L (2011) Recent advances in modeling and online detection of stator inter-turn faults in electrical motors. IEEE Trans Ind Electron 58(5):1564–1575
2. Nandi S, Toliyat HA, Li X (2005) Condition monitoring and fault diagnosis of electrical motors—a review. IEEE Trans Energy Convers 20(4):719–729
3. El Hachemi Benbouzid M (2000) A review of induction motors signature analysis as a medium for faults detection. IEEE Trans Ind Electron 47(5):984–993
4. Siddique A, Yadava GS, Singh B (2005) A review of stator fault monitoring techniques of induction motors. IEEE Trans Energy Convers 20(1):106–114
5. Acosta GG, Verucchi CJ, Gelso ER (2006) A current monitoring system for diagnosing electrical failures in induction motors. Mech Syst Signal Process 20(4):953–965
6. Thomson WT, Fenger M (2001) Current signature analysis to detect induction motor faults. IEEE Ind Appl Mag 7(4):26–34
7. Jung JH, Lee JJ, Kwon BH (2006) Online diagnosis of induction motors using MCSA. IEEE Trans Ind Electron 53(6):1842–1852
8. Kia SH, Henao H, Capolino GA (2009) Diagnosis of broken-bar fault in induction machines using discrete wavelet transform without slip estimation. IEEE Trans Ind Appl 45(4):1395–1404
9. Da Silva AM, Povinelli RJ, Demerdash NA (2008) Induction machine broken bar and stator short-circuit fault diagnostics based on three-phase stator current envelopes. IEEE Trans Ind Electron 55(3):1310–1318
10. Rangel-Magdaleno J, Romero-Troncoso R, Osornio-Rios RA, Cabal-Yepez E, Contreras-Medina LM (2009) Novel methodology for online half-broken-bar detection on induction motors. IEEE Trans Instrum Meas 58(5):1690–1698
11. Sun YG, Wang XH, Gui L, Wang WJ (2008) Simulation research on inter-turn short circuits of field windings in synchronous machines. Adv Technol Electr Eng Energy 27(2):5
12. Arkan M, Kostic-Perovic D, Unsworth PJ (2005) Modelling and simulation of induction motors with inter-turn faults for diagnostics. Electr Power Syst Res 75(1):57–66
13. Vaseghi B, Nahid-Mobarakh B, Takorabet N, Meibody-Tabar F (2011) Inductance identification and study of PM motor with winding turn short circuit fault. IEEE Trans Magn 47(5):978–981
14. Toma S, Capocchi L, Capolino GA (2013) Wound-rotor induction generator inter-turn short-circuits diagnosis using a new digital neural network. IEEE Trans Ind Electron 60(9):4043–4052
15. Faiz J, Ebrahimi BM, Akin B, Toliyat HA (2008) Finite element transient analysis of induction motors under mixed eccentricity fault. IEEE Trans Magn 44(1):66–74